PCCP

Cite this: *Phys. Chem. Chem. Phys.*, 2012, **14**, 14619–14629

www.rsc.org/pccp

PAPER

Dynamics due to combined buoyancy- and Marangoni-driven convective flows around autocatalytic fronts

M. A. Budroni,* L. Rongy* and A. De Wit*

Received 12th June 2012, Accepted 13th August 2012
DOI: 10.1039/c2cp41962a

A reaction–diffusion–convection (RDC) model is introduced to analyze convective dynamics around horizontally traveling fronts due to combined buoyancy- and surface tension-driven flows in vertical solution layers open to the air. This isothermal model provides a means for a comparative study of the two effects *via* tuning two key parameters: the solutal Rayleigh number Ra, which rules the buoyancy influence, and the solutal Marangoni number Ma governing the intensity of surface effects at the interface between the reacting solution and air. The autocatalytic front dynamics is probed by varying the relative importance of Ra and Ma and the resulting RDC patterns are quantitatively characterized through the analysis of the front mixing length and the topology of the velocity field. Steady asymptotic regimes are found when the bulk and the surface contributions to fluid motions act cooperatively *i.e.* when Ra and Ma have the same sign. Complex dynamics may arise when these numbers are of opposite signs and the two effects thus compete in an antagonistic configuration. Typically, spatiotemporal oscillations are observed as the control parameters are set in the region ($Ra < 0$, $Ma > 0$). Periodic behaviour develops here even in the absence of any double-diffusive interplay, which in previous literature was identified as a possible source of complexity.

1 Introduction

In spatially extended systems, autocatalytic reactions coupled to diffusion can trigger propagating chemical fronts.[1,2] This is one of the typical examples of spatiotemporal organisation of chemical systems out of equilibrium.[3] The intimate mechanism at the basis of stationary and dynamic chemical patterns is the coupling between nonlinear kinetics and mass transport phenomena. The active interplay between reaction and diffusion processes can give rise to chemical waves and fronts, and the study of these structures has traditionally been carried out in gels in order to avoid complications due to convective flows. Convective motions inevitably occur in aqueous solutions when propagating fronts self-sustain an interface between two miscible phases (the products and the fresh reactants respectively) because of density and surface tension gradients across the front. In past years many efforts have been devoted towards understanding how the mutual interaction between kinetics and convective transport phenomena enhances complex behaviours. The influence of bulk and surface flows on the front dynamics has been pointed out in both experimental[4–22] and theoretical works,[23–42] showing that chemical fronts can be distorted, accelerated or even broken by the hydrodynamic feedback. The reaction–diffusion–convection coupling has proved to be also responsible for order–disorder transitions in chemical oscillators, where it controls the route from periodic regimes to spatiotemporal chaos.[43] Nevertheless getting into a detailed understanding of chemo-hydrodynamic instabilities remains a challenging task when both surface and buoyancy effects concur at the same time to the convective motions. In this context a numerical approach is a powerful way for discriminating the relative weight of each contribution at play.

In a series of previous articles, we have theoretically investigated the separate role of either pure buoyancy or pure Marangoni solutal contributions in the fluid motions around autocatalytic fronts. The front dynamics was first considered in a thin closed reactor under isothermal conditions, where the different composition between the reacted and non-reacted solutions initiates buoyancy-driven flows due to horizontal gradients in density.[35] The deformation of the resulting chemo-hydrodynamic structures, with respect to the associated reaction–diffusion solution, depends on the direction and the magnitude of the density gradient $\Delta\rho = \rho_{products} - \rho_{reactants}$. In the presence of such pure solutal buoyancy effects, the set of possible dynamics is limited to asymptotically steady solutions. If the exothermicity of the reaction is taken into account, more complicated behaviours arise when both thermal and solutal contributions to the density variation come into play.[39,41] The two sources of buoyancy convection can indeed act cooperatively

Nonlinear Physical Chemistry Unit, Service de Chimie Physique et Biologie Théorique, Université Libre de Bruxelles (ULB), Faculté des Sciences, CP 231, 1050 Brussels, Belgium. E-mail: mbudroni@ulb.ac.be, lrongy@ulb.ac.be, adewit@ulb.ac.be

or in a competing way. As the autocatalytic reactions involved in chemical fronts are typically exothermic, traveling products are hotter than the reactants and therefore rise up to the top of the reactor, generating a clockwise vortex at the propagating interface. When the solute products are less dense than fresh reactants, the solutal and thermal contributions coherently deform the chemical structure, which results in a larger deformation. In contrast, if the solute products are denser than the reactant, the antagonism between thermal and solutal components can lead to oscillatory spatio-temporal structures so-called *rolling chemical fronts*. Dynamical behaviours obtained in numerical simulations for these various regimes are in good agreement with the experimental observations for the Iodate–Arsenous Acid (IAA) and the Chlorite–Tetrathionate (CT) reaction in closed reactors.[41]

Numerical studies have also analyzed pure Marangoni effects. In this case the front evolution is followed in thin solution layers open to the air and in the absence of any density gradient. As the front propagates, it supports a surface tension gradient, $\Delta\gamma = \gamma_{\text{products}} - \gamma_{\text{reactants}}$, generating a net force at the air–solution interface. The resulting surface flow is oriented towards the region with larger surface tension and, as the incompressible fluid is bounded, it also affects the bulk dynamics. Concentration and temperature changes can both singularly or cooperatively contribute to such surface tension gradients. When the autocatalytic front is coupled to the pure solutal Marangoni effect (*i.e.* under isothermal conditions), it leads to steady asymptotic dynamics, characterized by a flow vortex traveling at a constant speed with the front and deforming it.[33,34,36] After a transient period, which can also be oscillatory, the deformed front attains an asymptotic constant shape. Again, the introduction of the thermal contribution can induce a double-diffusive interplay and the emergence of complex spatio-temporal dynamics such as oscillatory patterns.[42]

While the separate role played by pure buoyancy-driven and pure surface-driven flows in chemical traveling fronts has thus been successfully understood, the combined effect of these two contributions still remains unexplored from a theoretical point of view, though this is a genuine situation encountered for fronts propagating in thin layers open to the air.

In this context our goal is to fill this gap by studying new dynamical scenarios caused by the combined action of both solutal surface and buoyancy-driven convection on isothermal autocatalytic front dynamics. We refer to a thin layer solution with an air–liquid interface on the top, in an ideally thermostated reactor, in which density and surface tension gradients develop across the traveling front because of the chemical composition changes. The dynamics of the system is described by a reaction–diffusion–convection (RDC) model, where evolution equations for the concentration of the autocatalytic product with cubic kinetics is coupled to Fickian diffusion and to the Navier–Stokes equations, governing the velocity of the fluid in the reactor. The surface effects are considered by introducing a Marangoni boundary condition at the free surface border while buoyancy-driven effects are parametrized by a Rayleigh number that appears in the dependence of the dimensionless density of the solution on the concentration of the product.

A detailed discussion of the model and of the numerical methods employed is given in Section 2. Solutal surface and buoyancy contributions to hydrodynamic motions can be either cooperative in which case they both trigger flows in the same direction or antagonistic if they yield flows of opposite directions. Here we develop a comparative investigation of the dynamics where the orientation and the intensity of the two effects can be parametrically controlled depending on the sign and amplitude of the Marangoni and Rayleigh number respectively. These aspects and the results of the numerical simulations are discussed at length in Section 3 and in the concluding remarks of Section 4.

2 Model and methods

We consider a two dimensional slab of length L_x and height L_z in a (x,z) reference frame. As sketched in Fig. 1, this represents a vertical cut in a 3-dimensional rectangular reactor, where the gravitational acceleration $\boldsymbol{g} = (0, -g)$ is oriented against the z axis and the chemical front propagates horizontally in the x direction.

In a previous paper,[41] we have explained how the reduction of the 3-dimensional problem to its 2-dimensional section does not affect the quality of the results with respect to experimental observations, capturing the essential mechanisms which favor chemo-hydrodynamic instabilities. The slab is supposed to be under isothermal conditions and open to the air at the top boundary (see an analogous experimental setup in ref. 21). The autocatalytic product, characterized by the density ρ_p and the surface tension γ_p, propagates towards positive x (from left to right here) invading the fresh reactant with density ρ_r and surface tension γ_r. The air–liquid interface is assumed to be non-deformable and evaporation is neglected.

The dynamics of the traveling front obeys a set of partial differential equations in which the chemical kinetics is coupled to diffusion *via* Fick's law and to natural convection by means of the incompressible Navier–Stokes equations, ruling the velocity field within the system.

The dimensional form of the RDC system is

$$\partial_t c + (\boldsymbol{v}\cdot\nabla)c = D\nabla^2 c + f(c) \qquad (1)$$

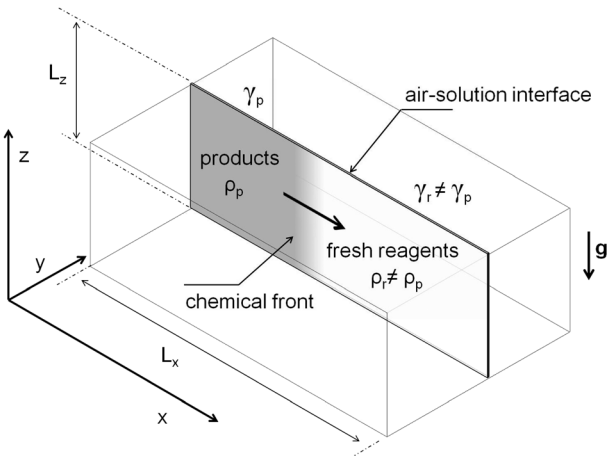

Fig. 1 Sketch of the vertical slab defining the spatial domain of our RDC model.

$$\partial_t \boldsymbol{v} + (\boldsymbol{v}\nabla)\boldsymbol{v} = -\frac{1}{\rho_0}\nabla p + \nu\nabla^2\boldsymbol{v} - g\frac{(\rho-\rho_0)}{\rho_0}\mathbf{1}_z \quad (2)$$

$$\nabla\cdot\boldsymbol{v} = 0. \quad (3)$$

We focus on a cubic kinetic function $f(c) = kc^2(a_0 - c)$, which derives from the general autocatalytic scheme

$$a + 2c \xrightarrow{k} 3c. \quad (4)$$

This kinetics is capable of sustaining traveling fronts between two different steady states when coupled to molecular diffusion and is fruitfully employed as a simple model for describing chemical clocks, such as the Iodate–Arsenous–Acid (IAA) reaction in a given range of starting reactant concentrations.[1,44] Here c identifies the concentration of the auto-catalytic species. Small initial traces of the product can trigger the front propagation through the substrate a. According to the mass conservation principle, the initial concentration of the reactant, a_0, can be used to replace the chemical variable a in the kinetic function as $a = (a_0 - c)$. Hydrodynamic equations are derived in the Boussinesq approximation,[45] assuming that density changes only affect the gravitational term $g\frac{(\rho-\rho_0)}{\rho_0}$ of eqn (2), where g is the gravitational acceleration and $\frac{(\rho-\rho_0)}{\rho_0}$ is the density variation due to the concentration change of the auto-catalytic species with respect to the initial reference state of the reactant (a_0, ρ_0). $\boldsymbol{v} = (u,v)^T$ is the velocity field, ν is the kinematic viscosity, D is the diffusion coefficient of the autocatalytic species, and p is the pressure.

We apply no-flux boundary conditions for the concentration at the four boundaries of our system and no-slip conditions for the velocity field at the three solid boundaries. To include the shear force at the free surface caused by surface tension effects, we apply the Marangoni condition to the horizontal component of the fluid velocity:

$$\mu\frac{\partial u}{\partial z} = \frac{\partial \gamma}{\partial x} \text{ at } z = L_z \quad (5)$$

where γ is the surface tension of the solution and μ the dynamic viscosity. We suppose a linear dependence between the surface tension and the surfactant concentration ($\gamma = \gamma_0 + (\mathrm{d}\gamma/\mathrm{d}c)c$, with γ_0 the initial surface tension of the solution and $\mathrm{d}\gamma/\mathrm{d}c$ constant). The vertical component v is set to zero because we assume an undeformable interface.

The system can be conveniently casted into a dimensionless form by using the timescale of the chemical process $t_0 = 1/(ka_0^2)$, and the reaction–diffusion characteristic length $L_0 = \sqrt{Dt_0}$. To have an order of magnitude of these scales, one can consider typical values for the IAA reaction:[1,44] for example, an initial concentration of the reactant (iodate) $a_0 = 5$ mM with the kinetic constant $k = 2 \times 10^4$ M^{-2} s^{-1} and $D \sim 2 \times 10^{-5}$ cm^2 s^{-1} give $t_0 \sim 2$ s and $L_0 \sim 0.01$ cm. From t_0 and L_0 the velocity, the pressure and concentration scales are derived as $v_0 = L_0/t_0 = \sqrt{D/t_0}$, $p_0 = \frac{\rho_0 L_0 v_0}{t_0}$ and a_0 respectively. The introduction of scaled variables gives the following dimensionless equations:

$$\partial_t c + (\boldsymbol{v}\cdot\nabla)c = \nabla^2 c + c^2(1-c) \quad (6)$$

$$\partial_t \boldsymbol{v} + (\boldsymbol{v}\cdot\nabla)\boldsymbol{v} = -\nabla p + S_c(\nabla^2\boldsymbol{v} - \mathrm{Ra}\, c\, \mathbf{1}_z) \quad (7)$$

$$\nabla\cdot\boldsymbol{v} = 0 \quad (8)$$

and allows to define dimensionless parameters. The Schmidt number, $S_c = \nu/D$, gives the balance between momentum and mass diffusion. In our simulations we set $S_c = 445$, since we refer to dynamics in aqueous solutions with the water kinematic viscosity $\nu = 0.0089$ cm^2 s^{-1} and usual values for the diffusivity of autocatalytic species in water $D \in (7 \times 10^{-6}, 2 \times 10^{-5})$ cm^2 s^{-1}. The solutal Rayleigh number Ra is defined as

$$\mathrm{Ra} = -\frac{1}{\rho_0}\frac{\partial\rho}{\partial c}\frac{a_0 {L_0}^3 g}{D\nu} \quad (9)$$

where $\frac{1}{\rho_0}\frac{\partial\rho}{\partial c}$ is the solutal coefficient in the linear expansion for the total density $\rho(c) = \rho_0\left[1 + \frac{1}{\rho_0}\frac{\partial\rho}{\partial c}(c - c_0)\right]$. Contrary to the conventional notation, where $\frac{\partial\rho}{\partial c}$ is assumed to be positive, here $\frac{\partial\rho}{\partial c} < 0$ (and Ra > 0) if products are less dense than the non-reacted medium, such as in the IAA reaction,[10] and $\frac{\partial\rho}{\partial c} > 0$ if the propagating products are denser than starting reactants, as it happens in the CT system.[40] Ra, one of the key parameters in our study, controls the solutal buoyancy contribution to convective flows and, hence, the coupling between natural buoyancy convection and the reaction–diffusion processes.

By taking the curl of both sides of eqn (7), the term ∇p can be eliminated. If we then define the *vorticity* as $\omega = \nabla \times \boldsymbol{v}$ and the *stream function*, ψ, through the relations $u = \partial_z\psi$ and $v = -\partial_x\psi$, we get the $(\omega - \psi)$ form of our RDC model

$$\frac{\partial c}{\partial t} + \left(\frac{\partial\psi}{\partial z}\frac{\partial c}{\partial x} - \frac{\partial\psi}{\partial x}\frac{\partial c}{\partial z}\right) = \nabla^2 c + c^2(1-c) \quad (10)$$

$$\frac{\partial\omega}{\partial t} + \left(\frac{\partial\psi}{\partial z}\frac{\partial\omega}{\partial x} - \frac{\partial\psi}{\partial x}\frac{\partial\omega}{\partial z}\right) = S_c\left(\nabla^2\omega - \mathrm{Ra}\frac{\partial c}{\partial x}\right) \quad (11)$$

$$\frac{\partial^2\psi}{\partial x^2} + \frac{\partial^2\psi}{\partial z^2} = -\omega. \quad (12)$$

The system (10–12) is solved by using the Alternating Direction Implicit Method (ADI) proposed by Peaceman and Rachford[46] which is particularly useful for two-dimensional problems. Briefly, this algorithm consists of solving explicitly the derivatives along one spatial dimension (let's say along the x axis) and implicitly in the second one (z). The direction along which the implicit and the explicit descriptions are employed is alternated during each successive iteration. At a given time step, the unknowns in each single equation are the implicitly calculated variables, so that the solution is reduced to handle a tridiagonal matrix.

We consider a spatial domain of dimensionless length $L_x = 512$ and height $L_z = 10$ (equivalent to a 5 cm $\times$ 0.1 cm solution layer), discretized over a grid of 1024×42 points. In other words, we use a horizontal mesh $hx = 0.5$ and a vertical mesh $hz = 0.25$. A finer grained discretization is required along the z-axis since the convective contribution initiated at the free border induces sharp gradients in this direction. The length of the system does not influence the simulations as long as it is taken sufficiently long for the front not to interact with a lateral boundary. On the other hand, the layer thickness L_z can be a determinant parameter for modulating

the buoyancy contribution and we will discuss this aspect in Section 3.

Zero-flux boundary conditions are imposed at each wall of the slab for the chemical field:

$$\frac{\partial c}{\partial x} = 0 \text{ at } x = 0;\ x = L_x \tag{13}$$

$$\frac{\partial c}{\partial z} = 0 \text{ at } z = 0;\ z = L_z \tag{14}$$

No-slip conditions, required at rigid walls for the flow, directly apply to the stream function as

$$\psi = \frac{\partial \psi}{\partial x} = 0 \text{ at } x = 0;\ x = L_x \tag{15}$$

$$\psi = \frac{\partial \psi}{\partial z} = 0 \text{ at } z = 0;\ z = L_z \tag{16}$$

From the no-slip boundary conditions, a second order form for the rigid wall vorticity can be derived according to Wood's formula,[47]

$$\omega|_x = -\frac{3\psi|_{x+hx}}{(hx)^2} - \frac{1}{2}\omega\Big|_{x+hx} \quad \text{at } x = 0 \tag{17}$$

$$\omega|_x = -\frac{3\psi|_{L_x-hx}}{(hx)^2} - \frac{1}{2}\omega\Big|_{L_x-hx} \quad \text{at } x = L_x \tag{18}$$

$$\omega|_z = -\frac{3\psi|_{z+hz}}{(hz)^2} - \frac{1}{2}\omega\Big|_{z+hz} \quad \text{at } z = 0. \tag{19}$$

At the free surface, the Marangoni boundary condition reads

$$\frac{\partial u}{\partial z} = -\mathrm{Ma}\frac{\partial c}{\partial x} \text{ at } z = L_z \tag{20}$$

or, in the ψ–ω formulation,

$$\omega = -\mathrm{Ma}\frac{\partial c}{\partial x} \text{ at } z = L_z \tag{21}$$

since, at $z = L_z$, $\omega = \frac{\partial u}{\partial z}$.

The solutal Marangoni number Ma, defined as:

$$\mathrm{Ma} = -\frac{1}{\mu\sqrt{kD}}\frac{\mathrm{d}\gamma}{\mathrm{d}c} \tag{22}$$

is our second key parameter. It is useful here to specify that when $\frac{\mathrm{d}\gamma}{\mathrm{d}c} > 0$ the product c increases the solution surface tension, which yields a net force oriented in the opposite direction with respect to the front motion. If $\frac{\mathrm{d}\gamma}{\mathrm{d}c} < 0$, the reacted solution presents a lower surface tension than the reactants and the front experiences a surface force along the direction of propagation.

A step function is set as the starting spatial distribution of the autocatalytic species $c(x,z,t)$ to initiate the front propagation:

$$c(x,z,0) = \begin{cases} 1 & \text{if } x < 50 \\ 0 & \text{elsewhere} \end{cases}$$

The numerical integration of the associated reaction–diffusion system is carried out until a front solution with characteristic speed $v_{RD} = 2\sqrt{2}$ and constant shape (front width $w_{RD} = 13$) is reached.[1] The resulting initial configuration of the front must prevent the system dynamics from boundary effects and from numerical instability due to initial sharp gradients of concentration. The coupling to the convective contributions is then effectively introduced. Calculations are run for 80 units of time, using the integration time step $ht = 1 \times 10^{-5}$. The stability of the numerical code was validated by comparing the integration performed for different values of Ma fixing Ra = 0 (and *vice versa*) with the results previously obtained.[33,35]

3 Results and discussion

The landscape of possible interplay between the buoyancy and surface effects on a front dynamics can be framed in the parameter plane (Ra,Ma) (Fig. 2). In this large parameter space, we can classify the main instability scenarios into four macro-regions: in quadrants I and III, where Ra and Ma have the same sign, the buoyancy and the Marangoni contributions to convective flow act in a cooperative way; in quadrants II and IV, the opposite sign of the two parameters corresponds to an anti-parallel configuration of the two convective contributions and, indeed, an effective antagonism. We probed the quantitative response of the front to variations in Ra and Ma by calculating the mixing length, L_m, which measures the distance between the tip and the back of the traveling front according to the formula:

$$L_m = x_{tip} - x_{back} \tag{23}$$

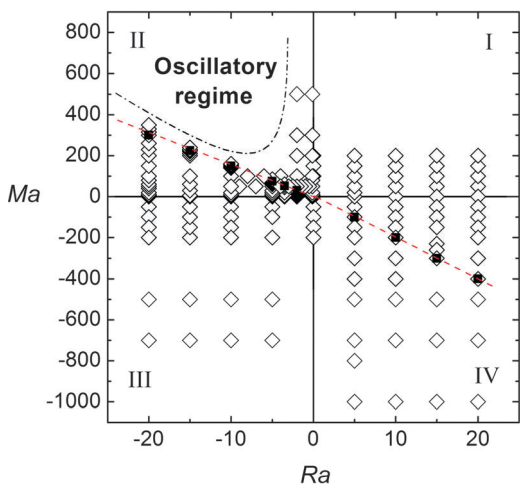

Fig. 2 Overview of the parameter space (Ra,Ma). Dynamical regimes for the asymptotic front mixing length, W, are reported as a function of Ra and Ma. Quadrants I and III encompass dynamics in which Marangoni and buoyancy effects are cooperative while in quadrants II and IV the two convective contributions observe an antagonist behavior. Empty diamonds represent asymptotic stationary solutions. Oscillatory dynamics are located in quadrant II. When the two effects are antagonistic but comparable, W stabilizes over a minimum, which scales linearly with Ra and Ma, as indicated by filled squares. No oscillatory behavior is observed in quadrant IV, even if the Marangoni and the buoyancy effects are antagonistic.

where the definition of x_{tip} and x_{back} is based on the transversely averaged value of the concentration profile $c(x,z,t)$ over the z-direction:

$$\langle c\rangle(x,t) = \frac{1}{L_z}\int_0^{L_z} c(x,z,t)\mathrm{d}z. \qquad (24)$$

The tip localises the position along x in front of which the depth-averaged concentration is less than 0.01, while the back corresponds to the position behind which the depth-averaged concentration is larger than 0.99. Typically, for a front horizontally propagating from left to the right (*i.e.* increasing values of x), $x_{back} = \min\{x: \langle c\rangle\ (x,t) \leq 0.99\}$ and $x_{tip} = \min\{x: \langle c\rangle\ (x,t) \leq 0.01\}$.

In the antagonistic cases it can be useful to relate the complexity of the front dynamics to the topology of the stream function. This describes the flow intensity and orientation at each point. ψ maxima localise counterclockwise flows while ψ minima indicate domains where convective motions follow a clockwise direction. The idea is that increasing the number of convective rolls due to the competing interplay between Marangoni and buoyancy effects corresponds to increasing complexity in the front dynamics. To this end, we calculate the minima and the maxima of the ψ function by classifying critical points of ψ (*i.e.* points where $\nabla\psi = 0$) on the basis of the eigenvalues of the Hessian matrix, $\mathbb{H}$: if the matrix is positive a critical point is a minimum; *vice versa*, if it is negative, the point can be addressed as a local maximum. The spatiotemporal dynamics of these reference points is compared and related to the chemical structure.

Ra > 0, Ma > 0

We first consider dynamics ruled by positive Rayleigh and Marangoni solutal numbers (quadrant I). The velocity field derives from a clockwise component around the front induced by the denser reactants sinking under the products as the front travels and from a net force at the surface, oriented along the direction of the front propagation. As a result the chemical structure is elongated towards the top of the reactor, with a deformation which grows as a function of the absolute value of the control parameters. In Fig. 3c we show a typical convective deformation of an autocatalytic front affected by this cooperative interplay after a transient period following which a stable conformation sets in. The illustration shows a concentration map of the chemical front, with the reacted solution on the left ($c = 1$) (in red online) and the fresh reactants on the right ($c = 0$) (in blue online). The asymptotic hydrodynamic configuration consists of one unique convective roll, localized across the deformed front and moving with it at a constant speed. Keeping Ra fixed, the mixing length L_m increases with Ma and it always reaches an asymptotic steady regime, characterized by the constant mixing length value W, after a monotonically increasing transient. The length of the transient period does not show any strict dependence on the variation of the control parameter (Fig. 3a). Direct information about the trend traced by asymptotic solutions as a function of Ma is displayed in Fig. 3b: W(Ma) describes a monotonically increasing curve which can be linearly fitted as $W = (0.275 \pm 0.004)\mathrm{Ma} + (116.8 \pm 0.5)$. Similar scalings are obtained for other values of Ra as well.

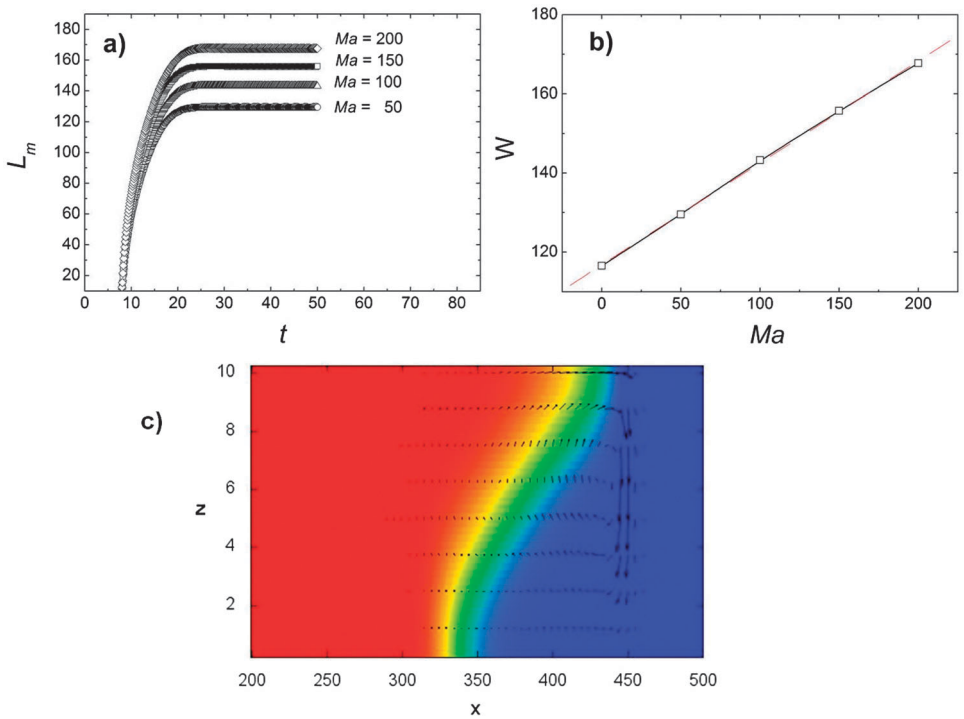

Fig. 3 Detailed analysis of quadrant I. (a) Front mixing length, L_m, as a function of time for different Ma $\in$[50,200] and Ra = 20. (b) Asymptotic values of the front mixing length, W, as a function of Ma. The curve describes a linear trend, according to $W = (0.275 \pm 0.004)\mathrm{Ma} + (116.8 \pm 0.5)$. (c) A snapshot of a typical RDC structure obtained for the cooperative combination (Ra = 5, Ma = 200). On the left (red online) is the autocatalytic species propagating into the reactants on the right (in blue online). The front is deformed by a single clockwise convective roll.

This scenario well describes the common behavior generally followed by chemical fronts in the IAA reaction, when performed in excess of iodate. Here one of the main products, I_2, is known to lower the surface tension, while the propagating products are less dense than non-reacted solution, thus promoting the condition for a positive cooperation and, indeed, a front shape as in Fig. 3c.

Ra < 0, Ma < 0

Analogous considerations can be drawn for the dynamical regimes obtained when both control parameters are negative. In this case the cooperative counter-clockwise interplay between the bulk and surface effects on the fluid motion originates from the denser product sinking below the less dense non-reacted solution, and from the surface force due to the larger surface tension of the products with respect to that of the reactants. Fig. 4c shows a convex shaped front, slowed down at the top of the layer, as imposed by the single counter-clockwise convective roll deforming the front. No symmetry with these structures and those obtained in the previous cooperative case can be recognized. Varying Ra in the range [−20,0] and Ma in [−200,0], the system always saturates to an asymptotic dynamical regime, characterized by a definite front speed and shape. These features are illustrated in Fig. 4a and b. Again a linear dependence of the asymptotic mixing length as a function of Ma can be extrapolated by the form $W = (-0.066 \pm 0.001)\mathrm{Ma} + (87.8 \pm 0.2)$. Similar trends can be obtained for other values of Ra.

Ra < 0, Ma > 0

More complicated spatio-temporal behaviours can be found when the system is set in quadrant II of the parameter-space (Ra,Ma) (see Fig. 5), when the buoyancy and the surface contributions act in a competing way. This region describes a physical situation where products are denser than the reactants, which in turn present a larger surface tension. The result is that the surface force, directed coherently with the front propagation, is anti-parallel to the counter-clockwise convective component driven around the interface by the buoyancy effect. Looking at the temporal evolution of the mixing length *versus* time for different values of the solutal Marangoni number and fixed solutal Rayleigh number, it can be noticed that stationary solutions are no more the only ones allowed. The curves L_m(Ma) present a transient to the final stable dynamics which strongly depends on the variation of Ma.

In Fig. 5a we report a typical example for Ra = −5. A characteristic non-monotonic trend in the asymptotic mixing length is found by plotting *W versus* Ma (Fig. 5b). This behavior shows a direct correspondence with the spatial distribution of chemical concentration shown in Fig. 5c. When Ma tends to zero, the front shape and the magnitude of the deformation is dictated by the dominating influence of solutal buoyancy effects and the front is elongated at the bottom of the spatial domain (see top of Fig. 5c). As the surface contribution grows in intensity, the related convective roll working at the upper part of the chemical interface comes

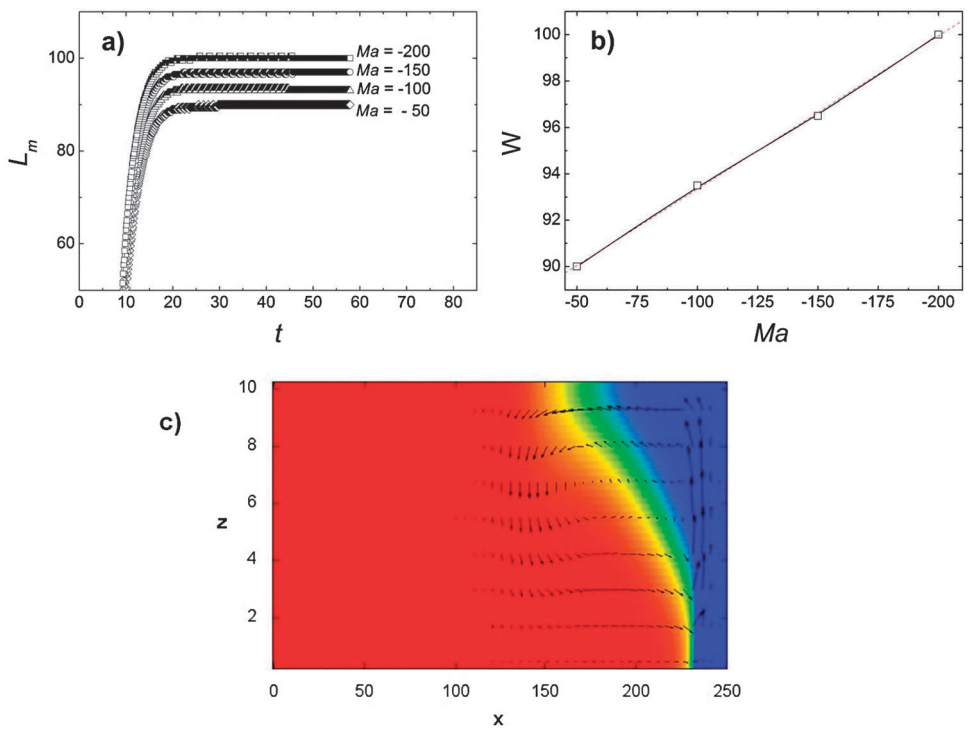

Fig. 4 Detailed analysis of quadrant III. (a) Front mixing length, L_m, as a function of time for different Ma ∈ [−200, −50] and Ra = − 20. (b) Asymptotic values of the front mixing length, W, as a function of Ma. The curve describes a linear trend according to $W = (-0.066 \pm 0.001)\mathrm{Ma} + (87.8 \pm 0.2)$. (c) Magnification of a typical steady RDC structure obtained for the cooperative combination (Ra = −20, Ma = −200). On the left (in red online) is the autocatalytic species propagating into the fresh reactants on the right (in blue online). The front is deformed by a single counterclockwise convective roll.

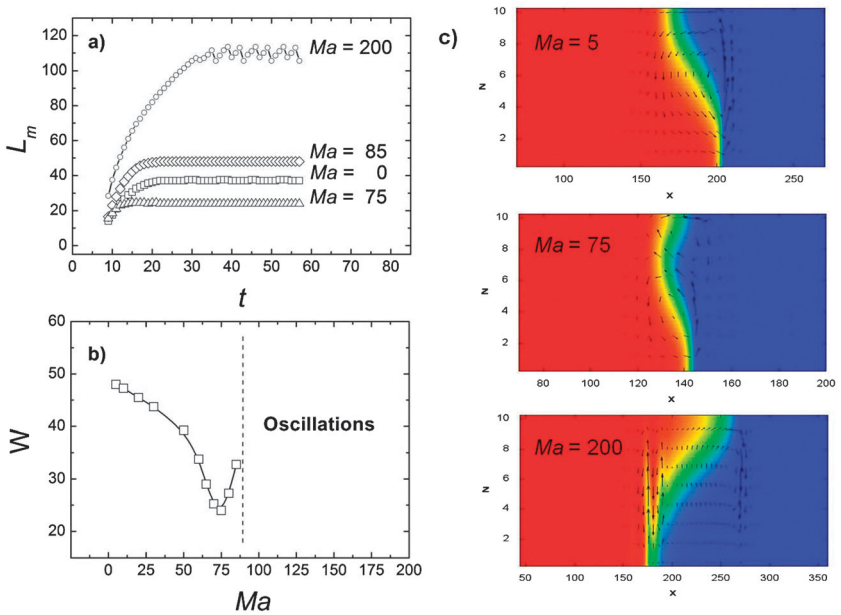

Fig. 5 Detailed analysis of quadrant II. (a) Time series of the mixing length, L_m *versus* Ma in the antagonistic region (Ra < 0, Ma > 0), for Ra = −5; (b) Characteristic trend traced by the asymptotic solutions W as a function of Ma. The curve exhibits a minimum at Ma = 75, where the competing contributions to the convective motions induced by the buoyancy and the surface components are comparable and result in a flattening effect. In the Ma-domain lower than W-minimum the buoyancy effect is dominating while for Ma > 75 the surface effect drives the front dynamics. Beyond the critical threshold Ma = 85, the system undergoes spatiotemporal oscillations; (c) the transition from the buoyancy-controlled to the Marangoni-controlled spatiotemporal structures is followed reporting the asymptotic solutions for Ma = 5, Ma = 75 and Ma = 200, when Ra = −5. The magnification of the structures at the front position shows that when Ma = 5 there is one main convective roll deforming the interface. In the second picture two main anti-parallel vortexes rule the wave deformation. A more complicated hydrodynamic configuration emerges for Ma > 85.

into play and compensates the action of the convective flow induced in the bulk by the density changes. The effect is to flatten the front, decreasing W (see middle of Fig. 5c). Hence a minimum in W which can be observed in the curve W(Ma) (Ma = 75 for Ra = − 5) occurs at the condition where the solutal buoyancy and Marangoni effects have comparable importance. For larger values of Ma, the surface effect prevails and the front switches to a shape much more elongated at the top of the reactor (see bottom of Fig. 5c). Nevertheless the buoyancy influence is not completely negligible and the combined antagonistic action of the two components leads to an oscillatory behavior, as revealed by the dynamics $W(t)$ for Ma = 200. Oscillations at the autocatalytic front occur because the local region of solute denser product, brought on top of the less dense non-reacted fluid by the Marangoni surface flow, starts sinking under the influence of the gravitational field, forming a finger. The timescale at which this tongue moves down along the z-direction is comparable to that of the main front propagation, so that they can get in touch. When the tongue and the main front join together, the smooth dynamics of the rear of the front undergoes a sharp jump in the x position consistent with a decrease in W. In the upper panel of Fig. 6, we sketch three typical configurations of the chemical front describing one cycle of the oscillatory dynamics. The correspondent hydrodynamic evolution is shown in the lower panel of Fig. 6, where we report the contour lines of the stream function for the same moments as for the chemical structures in the upper panel. Here the triangles indicate ψ minima (clockwise vortexes) while squares locate ψ maxima (counterclockwise vortexes). The spatiotemporal dynamics of ψ highlights how the tongue formation at the front is associated with the temporary emergence of new clockwise and counterclockwise rolls, which eventually vanish as the tongue and the main front annihilate. The formation (and extinction) of convective rolls solely interests the bulk of the system and, in particular, affects the dynamics of the back of the front. On the other hand, the tip, located at the air–liquid interface, experiences a constant action of a clockwise vortex related to the Marangoni contribution. This mechanism of emergence–annihilation of the tongue reiterates in time, justifying the periodic changes in the front mixing length. On top of this qualitative explanation, in Fig. 7 we give a general overview of the relationship between (a) the tip and the back dynamics and (b) the number and the position of the hydrodynamic critical points. The same system as in Fig. 6 (Ra = −5, Ma = 200) is considered. While the evolution of the tip is completely smooth during the front propagation, the spatiotemporal plot associated with the back position traces a stairway behavior (Fig. 7a). This spatiotemporal topology coincides with that shown in Fig. 7b, where the dynamics of each counterclockwise (squares) and clockwise (triangles) convective roll is followed by staking its x-position as a function of time. After an induction period, several hydrodynamic structures coexist close to the reacting interface. One clockwise vortex located around the tip (straight curve in the graph) is preserved during all the simulations, whereas clockwise and counterclockwise rolls located at the front back periodically form and disappear, determining an oscillating

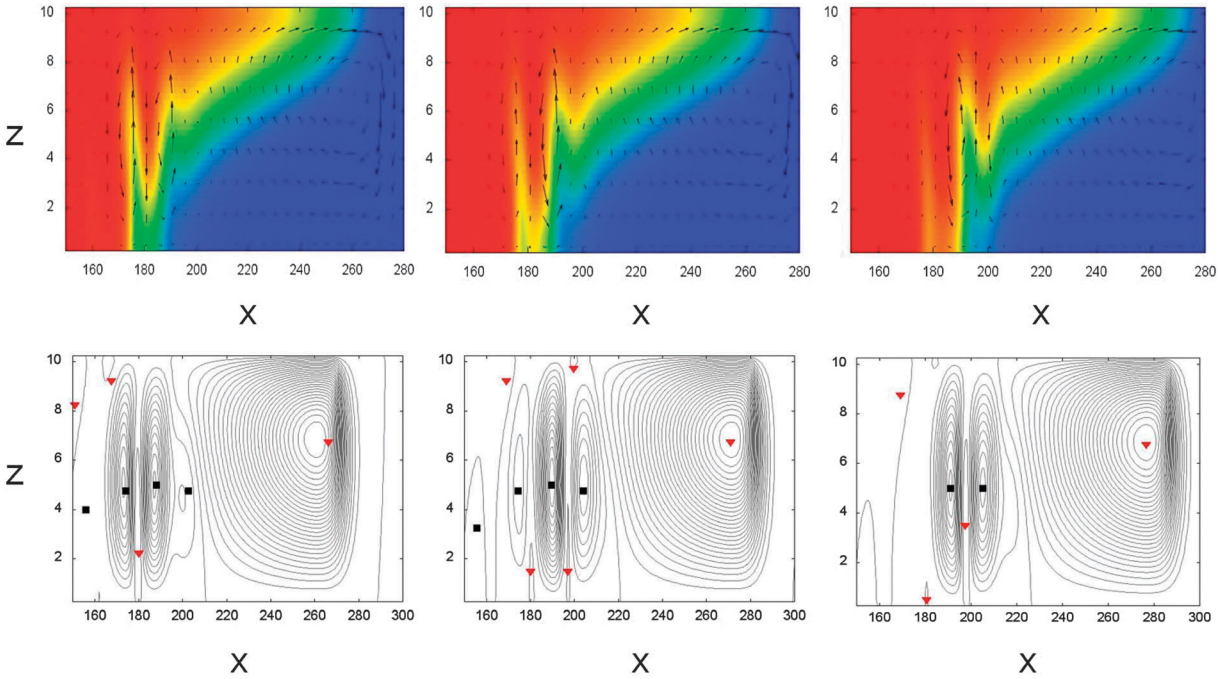

Fig. 6 Schematic of the basic mechanism at the origin of the oscillatory behaviour. In the upper panel we report snapshots of the chemical front at three salient instants (42, 44, 45 time units), in which a tongue along the z axis forms and annihilates. The periodic formation–annihilation of the tongue mainly affects the dynamics of the back of the front. The dynamical behavior of the hydrodynamic structures is shown in the lower panel by reporting the configuration of the stream function associated with the basic steps of the oscillatory mechanism. ψ minima, indicating clockwise convective rolls, are identified by triangles (red online) while squares (black online) locate ψ maxima, corresponding to counterclockwise rolls.

number of convective rolls and, more importantly, the stepwise dynamics also traced by the front back dynamics. The different behavior at the tip and at the back of the front makes it impossible to unambiguously define the front speed. The slope of the linear trend outlined by the tip (and by the related clockwise roll) gives the constant speed, while it turns to be oscillatory if we consider as a reference point the back of the front.

The transition to the oscillatory regime takes place beyond a characteristic threshold of Ma (Ma = 85 in Fig. 5), which linearly depends on the magnitude of the solutal Rayleigh number. The linear dependence exhibited by the critical threshold for the transition to oscillations is a manifestation of the intimate self-affinity which relates W dynamics to the key parameters. Fig. 8 shows the evident similarity among the curves obtained by plotting W(Ma) for different Ra. The scaling law relating these trends can be quantitatively captured by following the position of a reference point in the curves (for example the bifurcation point from stationary to oscillatory asymptotic solutions or the W(Ra,Ma) minimum) as Ra and Ma are changed.

The linear scaling obeyed by W(Ra,Ma) minima for Ra < 0 and Ma > 0 is highlighted in the II quadrant of Fig. 2 with filled squares. The fitting, according to the form Ma $= \alpha$Ra, reveals the coefficient $\alpha = -15$. Uncovering intrinsic self-similarities in the system observables is nowhere near a mere theoretical speculation. Assuming that the linear scaling also holds for larger values of the control parameters, we would be able, for instance, to predict critical conditions where surface and buoyancy effects are comparable or where oscillations can occur, whereas numerical calculations are prohibitive or even inaccessible due to the code stability.

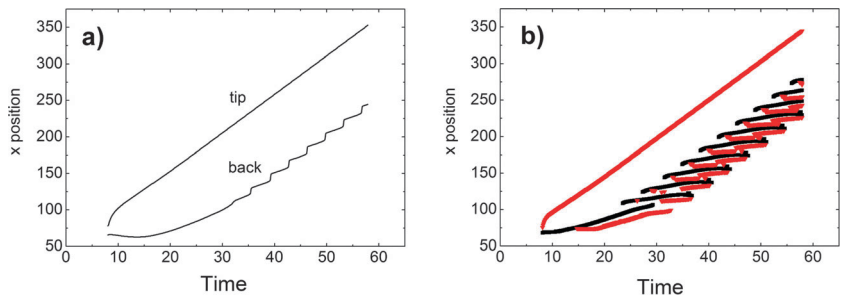

Fig. 7 Comparison between the dynamics of the tip and the back of the front (panel (a)) and the space–time plot tracing the behavior of convective rolls (panel (b)) in the oscillatory regime (Ra = −5, Ma = 200). In panel (b), squares (black online) and triangles (red online) identify the position of counterclockwise and clockwise vortexes respectively (see also Fig. 6 and discussion in the text).

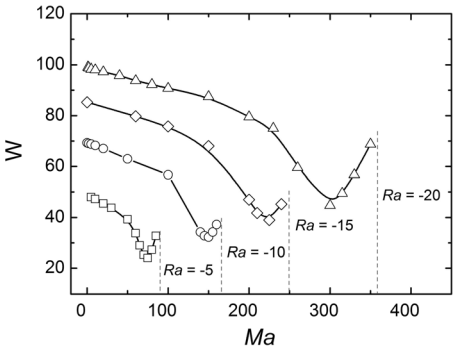

Fig. 8 Self-similar trends exhibited by W as a function of Ma for different values of Ra. Characteristic Ma values for each curve are those of the minimum in W (filled squares in Fig. 2) and the critical threshold beyond which oscillations occur (dashed lines at the end of each curve and dashed-dotted curve in the II quadrant of Fig. 2). The linear scaling relating these curves is discussed in the text.

Clearly, the mutual influence between bulk and surface-driven flows is the core of the oscillatory mechanism. Since the layer thickness can affect this force balance, we also investigate the role played by this parameter. We consider three values for the reactor height: $L_z = 5$, 8 and 12 in addition to $L_z = 10$ used until now. There is a sharp dependence of the critical Ma at which the transition from stationary to periodic behavior occurs, upon L_z. Below the threshold $L_z = 10$, no oscillations can be detected over the wide Ma domain considered (Ma $\in$ (0,500)), indicating that, for small layer thicknesses, any value of Ma > 0 is sufficient to make the surface effect dominant with respect to the buoyancy one. This is something expected since it is well known from theoretical works and experiments[27] that natural convection is hindered in reactors smaller than a characteristic spatial length. On the contrary, increasing L_z increases the relative importance of bulk effects, so that Ma values necessary for triggering the oscillatory dynamics are larger. As a result, the bifurcation point is shifted from Ma = 85 to Ma = 150 when L_z is increased from 10 to 12.

It is of great interest to consider the value and the correspondence of these numerical outcomes with experimental systems. In this context the CT reaction carried out under isothermal conditions would be a good candidate for testing the predicted oscillatory instability, since it at least fulfills the requirement of propagating products to be denser than the non-reacted substrate. Unfortunately no quantitative information about the behavior of this system in open reactors is well-established until now.

Ra > 0, Ma < 0

The previous oscillatory instability and similar scenarios observed in the literature[42] could suggest that an antagonism between two contributions to the convective flow is a sufficient condition for the emergence of spatio-temporal complexity. This is not true in general and our simulations using positive Rayleigh numbers and negative Marangoni numbers stand for a particular example which nullifies this hypothesis. Here the two contributions are anti-parallel since the less dense products tend to rise up to the top of the reactor inducing a density-driven clockwise flow across the front while the surface force points in the opposite direction, due to the larger surface tension of the products with respect to the non-reacted solution.

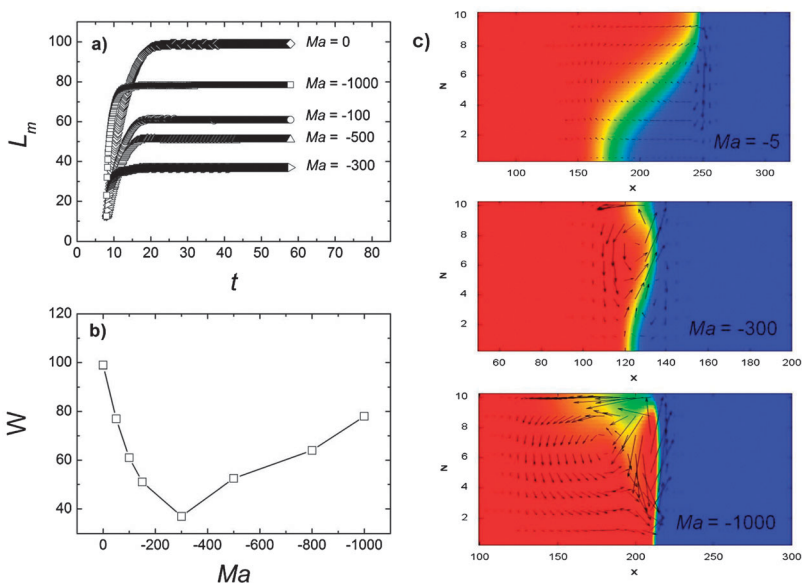

Fig. 9 Detailed analysis of quadrant IV. (a) Time series of the mixing length, L_m *versus* Ma in the antagonistic region (Ra > 0, Ma < 0), for Ra = 15; (b) characteristic trend traced by the asymptotic solutions W as a function of Ma. The curve exhibits a minimum close to Ma $= -300$, where the antagonistic contributions to the convective flow are comparable and result in a flattening effect. In the Ma domain lower than the W-minimum, the buoyancy effect is the dominating contribution while for Ma > 100 the surface effect is the leading force. No oscillations can be detected over the (Ra,Ma)-domain considered; (c) the transition from buoyancy to Marangoni-controlled structures is followed reporting the asymptotic solutions for Ma $= -5$, Ma $= -300$ and Ma $= -1000$ from top to bottom. The magnification of the structures at the front position shows that in the first structure there is one main convective roll deforming the front. In the second picture two main anti-parallel vortexes rule the wave deformation. A more complicated hydrodynamic configuration emerges for Ma < -300.

The resulting chemical structures depend on the leading contribution to convection as seen when plotting the asymptotic mixing length W as a function of Ma for fixed Ra (see Fig. 9b where Ma $\in$ [−1000,0] and Ra = 15). Steady states are attained with different velocities, depending on the magnitude of Ma. On the contrary, in the cooperative cases, the initial transients are not affected by changes in the value of the control parameters. The asymptotic condition is quickly reached for Ma = −300, where W(Ma) exhibits a minimum. This point separates the buoyancy and the surface-dominating region. Steady fronts much more elongated at the top of the layer are the typical structures for low Marangoni numbers (Fig. 9c, upper snapshot), while increasing the surface force renders the front convex in the middle of the reactor, as the top part of the front is "slowed" down (Fig. 9c, middle snapshot). Basically there are two convective rolls governing these dynamics for low absolute values of the Marangoni number. At larger surface forces, a more complex hydrodynamic configuration underlies the front dynamics (see the velocity field for Ma = −1000 in Fig. 9c).[36] No complex behavior is pointed out over the large section of the parameter space analyzed. We suspect that, in the range of values considered, we cannot achieve a sufficient deformation of the front to trigger the synergy between bulk and surface forces needed for oscillations as met in the region (Ra < 0 and Ma > 0). Also for this antagonistic case (Ra > 0, Ma < 0), an evident self-similarity is identified in the W(Ra,Ma) trends. This is indicated by the linear fitting of filled squares in the quadrant IV, which locates W(Ra,Ma) minima as a function of Ra and Ma. While the solutal buoyancy component is symmetric to the change of sign in $\Delta\rho$ as demonstrated in ref. 35 the solutal Marangoni effect is not symmetric with respect to $\Delta\gamma$.[33] This fact introduces in quadrant IV a different scaling of W as a function of Ra and Ma with respect to what we have seen for Ra < 0, Ma > 0. W-minima follow the trend Ma = (−19.6 ± 0.5)Ra. Physically, this implies that the surface contribution required to compensate the opposite effect of the buoyancy component (for instance for |Ra| = 5) is larger (|Ma| = 100) here than in the previously considered antagonistic case Ra > 0, Ma < 0 (|Ma| = 75).

The scenario Ra > 0, Ma < 0 gains particular interest if related to the front evolution observed experimentally in the IAA reaction, when performed in large excess of arsenous acid. In this case, I_2, which is the species lowering the surface tension, is an intermediate quickly consumed, and other species must act as the leading surfactants in the system, evidently increasing the surface tension in the region already "burnt" by the front. Even if the actual mechanism procuring such a superficial contribution is not well established, the arising structures closely remind those found for Ma = −1000 in Fig. 9c.

4 Conclusions

Propagating autocatalytic fronts are suitable model systems for studying hydrodynamic motions at a reactive self-sustained interface between two miscible liquids (products and reactants) with different densities and surface tensions. The arising convective flows feedback with the reaction dynamics, modifying the reaction-diffusion structures and defining different convective modes than those obtained in the non-reactive case. Interestingly, transport phenomena do not act here as homogenization agents, but actively couple with the nonlinear kinetics to trigger RDC spatiotemporal self-organization. The sources of convection are multiple, the most important ones being the thermal and solutal buoyancy effects and thermal and solutal Marangoni effects. Our project is to approach the emergence of complexity around chemical fronts by means of a parametric study which allows for a direct modulation of the mutual influence of surface and buoyancy contributions and to discriminate their relative weight in the global behavior. The work developed in this context up to now has been mainly focused on studying the separate role played by either pure gravitational or pure surface effects. Interestingly it was found that the introduction of double diffusive interplay,[39] such as that of solutal and thermal contributions to the flow can be a source of spatiotemporal complexity, as they can act in an antagonistic way at suitably different timescales. The numerical results agreed with "*ad hoc*" experiments carried out on the Iodate–Arsenous Acid and Chlorite–Tetrathionate systems, to point out the influence of hydrodynamic flows in the dynamics of propagating waves.[41]

Framed in the same scientific problem, this paper is not only a complement to previous efforts but a significant step in advance. As a matter of fact, this is a first attempt to explore the chemo-hydrodynamic instabilities when buoyancy and surface contributions are simultaneously taken into account. An overview of emerging scenarios can be set in the (Ra,Ma) parameter space, as sketched in Fig. 2, where Ra and Ma, respectively, control the buoyancy and the surface effect. Here the system response to the variation of the parameters Ra and Ma is considered over a significant extent of the parameter space and is characterized by means of the asymptotic mixing length W. This observable provides a quantitative measure of the front deformation under hydrodynamic influence. When Ra and Ma have the same sign, both effects exert a coherent contribution to convective instability and only stationary asymptotic dynamics are revealed from numerical integration of the RDC system. A chance for complex behaviors is given when the surface and the buoyancy components are antagonistic, namely in the region where Ra and Ma present opposite sign. One of the main results of our simulations is that such antagonism can lead to oscillatory dynamics in chemical clocks even in the absence of any double diffusive interplay. For Ra < 0 and Ma > 0, beyond a characteristic threshold of the control parameters, periodic changes in the front structure are observed and the rationalization of the oscillatory mechanism points out the necessity of an active synergy between the two convective contributions in play, without one being exclusively dominant. This point is confirmed by the strict dependence of the transition from steady to oscillatory solutions upon L_z. The layer thickness can effectively tune the strength of the coupling: the relative influence of buoyancy-driven flow is almost nullified by decreasing L_z under the threshold L_z = 10 and, *vice versa*, amplified by increasing it. In the first case the possibility for oscillatory behavior is suppressed since the Marangoni effect is the only one in play, while higher values of the layer thickness determine a shift to a

higher domain of the critical Ma necessary for sustaining the oscillatory mechanism.

One more possibility for a competing interplay between the solutal Marangoni effect and buoyancy driven flow is Ra $>$ 0 and Ma $<$ 0. No complex dynamical pattern results from our calculations (in the region of the parameter space considered), suggesting that antagonism between the surface and buoyancy effects is not a sufficient condition for complicated dynamics to occur. In both antagonistic cases, it turns out that the dynamics is pervaded by a linear scaling which relates the front observables in the (Ra,Ma)-space. Some of the known experimental observations can be directly mapped and understood in the taxonomy of possible instabilities developed until now in our theoretical studies. Well-established examples are the behavior of the IAA and the CT reaction. New experiments to validate instabilities predicted by numerical simulations can be designed following this pilot study, such as the birth of spatiotemporal oscillations in fronts where products are denser than fresh reactants and decrease the surface tension. In this regard the CT reaction appears to be a good candidate. The RDC scheme used in this investigation is a first step in view of a comprehensive model where both surface and buoyancy effects are included, taking into account thermal contributions too.

References

1 R. J. Field and M. Burger, *Oscillations and Traveling Waves in Chemical Systems*, Wiley, New York, 1985.
2 R. Kapral and K. Showalter, *Chemical Waves and Patterns*, Kluwer Academic Publishers, Dordrecht, Boston and London, 1994.
3 G. Nicolis and I. Prigogine, *Self-Organization in Nonequilibrium Systems*, Wiley, New York, 1977.
4 K. I. Agladze, V. I. Krinsky and A. M. Pertsov, *Nature*, 1984, **308**, 834–835.
5 G. Bazsa and I. R. Epstein, *J. Phys. Chem.*, 1985, **89**, 3050.
6 I. Nagypal, G. Bazsa and I. R. Epstein, *J. Am. Chem. Soc.*, 1986, **108**, 3635.
7 H. Miike, S. C. Müller and B. Hess, *Phys. Rev. Lett.*, 1988, **61**, 2109–2112.
8 H. Miike, S. C. Müller and B. Hess, *Chem. Phys. Lett.*, 1988, **144**, 515–520.
9 J. A. Pojman and I. R. Epstein, *J. Phys. Chem.*, 1990, **94**, 4966–4972.
10 J. A. Pojman, I. R. Epstein, T. J. McManus and K. Showalter, *J. Phys. Chem.*, 1991, **95**, 1299.
11 H. Miike, H. Yamamoto, S. Kai and S. C. Müller, *Phys. Rev. E*, 1993, **48**, R1627.
12 I. P. Nagy, A. Keresztessy, J. A. Pojman, G. Bazsa and Z. Noszticzius, *J. Am. Chem. Soc.*, 1994, **98**, 6030.
13 A. Keresztessy, I. P. Nagy, G. Bazsa and J. A. Pojman, *J. Phys. Chem.*, 1995, **99**, 5379.
14 B. S. Martincigh and R. H. Simoyi, *J. Phys. Chem. A*, 2002, **106**, 482.
15 G. Schuszter, T. Tóth, D. Horváth and A. Tóth, *Phys. Rev. E*, 2009, **79**, 016216.
16 J. Martin, N. Rakotomalala, L. Talon and D. Salin, *Phys. Rev. E*, 2009, **80**, 055101.
17 I. Bou Malham, N. Jarrige, J. Martin, N. Rakotomalala, L. Talon and D. Salin, *J. Chem. Phys.*, 2010, **133**, 244505.
18 T. Rica, E. Pópity-Tóth, D. Horváth and A. Tóth, *Physica D (Amsterdam)*, 2010, **239**, 831.
19 E. Pópity-Tóth, D. Horváth and A. Tóth, *J. Chem. Phys.*, 2011, **135**, 074506.
20 O. Miholics, T. Rica, E. Popity-Tóth, D. Horvóth and A. Tóth, *J. Chem. Phys.*, 2011, **135**, 204501.
21 L. Šebestíková and M. J. Hauser, *Phys. Rev. E*, 2012, **85**, 036303.
22 F. Rossi, M. A. Budroni, N. Marchettini and J. Carballido-Landeira, *Chaos*, 2012, DOI: 10.1063/1.4752194.
23 T. Plesser, H. Wilke and K. H. Winters, *Chem. Phys. Lett.*, 1992, **200**, 158.
24 D. A. Vasquez, J. W. Wilder and B. F. Edwards, *J. Chem. Phys.*, 1993, **98**, 2138–2143.
25 D. A. Vasquez, J. M. Littley, J. W. Wilder and B. F. Edwards, *Phys. Rev. E*, 1994, **50**, 280.
26 H. Wilke, *Physica D (Amsterdam)*, 1995, **86**, 508.
27 Y. Wu, D. A. Vasquez, B. F. Edwards and J. W. Wilder, *Phys. Rev. E*, 1995, **51**, 1119.
28 K. Matthiessen and S. C. Müller, *Phys. Rev. E*, 1995, **52**, 492.
29 K. Matthiessen, H. Wilke and S. C. Müller, *Phys. Rev. E*, 1996, **53**, 6056.
30 M. Diewald, K. Matthiessen, H. Wilke, S. C. Müller and H. R. Brand, *Phys. Rev. Lett.*, 1996, **77**, 4466.
31 V. Pérez-Villar, A. P. Munuzuri and V. Pérez-Munuzuri, *Phys. Rev. E*, 2000, **61**, 3771.
32 M. Belk, K. G. Kostarev, V. Volpert and T. M. Yudina, *J. Phys. Chem. B*, 2003, **107**, 10292–10298.
33 L. Rongy and A. De Wit, *J. Chem. Phys.*, 2006, **124**, 164705.
34 L. Rongy and A. De Wit, *J. Eng. Math.*, 2007, **59**, 221–227.
35 L. Rongy, N. Goyal, E. Meiburg and A. De Wit, *J. Chem. Phys.*, 2007, **127**, 114710.
36 L. Rongy, A. De Wit and G. M. Homsy, *Phys. Fluids*, 2008, **20**, 072103.
37 N. Jarrige, I. Bou Malham, J. Martin, N. Rakotomalala, D. Salin and L. Talon, *Phys. Rev. E*, 2010, **81**, 066311.
38 M. A. Budroni, M. Masia, M. Rustici, N. Marchettini, V. Volpert and P. C. Cresto, *J. Chem. Phys.*, 2008, **128**, 111102.
39 L. Rongy and A. De Wit, *J. Chem. Phys.*, 2009, **131**, 184701.
40 J. D'Hernoncourt, A. Zebib and A. De Wit, *Chaos*, 2007, **17**, 013109.
41 L. Rongy, G. Schuszter, Z. Sinkó, T. Tóth, D. Horváth, A. Tóth and A. De Wit, *Chaos*, 2009, **19**, 023110.
42 L. Rongy, P. Assemat and A. De Wit, *Chaos*, 2012, DOI: 10.1063/1.4747711.
43 M. A. Budroni, M. Masia, M. Rustici, N. Marchettini and V. Volpert, *J. Chem. Phys.*, 2009, **130**, 024902.
44 A. Hanna, A. Saul and K. Showalter, *J. Am. Chem. Soc.*, 1982, **104**, 3838.
45 J. Boussinesq, *Théorie Analytique de la Chaleur*, Gauthier-Villars, Paris, 1903, vol. 2.
46 D. W. Peaceman and H. H. Rachford, *J. Soc. Ind. Appl. Math.*, 1955, **3**, 28–41.
47 L. C. Woods, *Aero. Quart.*, 1954, **5**, 176.